arXiv:1411.1327v2 [cond-mat.str-el] 22 May 2015

Variational Monte Carlo study of chiral spin liquid in the extended Heisenberg model on the Kagome lattice

Wen-Jun Hu,[1] Wei Zhu,[1] Yi Zhang,[2] Shoushu Gong,[1] Federico Becca,[3] and D. N. Sheng[1]
[1] *Department of Physics and Astronomy, California State University, Northridge, California 91330, USA*
[2] *Department of Physics, Stanford University, Stanford, California 94305, USA*
[3] *Democritos National Simulation Center, Istituto Officina dei Materiali del CNR, and SISSA-International School for Advanced Studies, Via Bonomea 265, I-34136 Trieste, Italy*

We investigate the extended Heisenberg model on the Kagome lattice by using Gutzwiller projected fermionic states and the variational Monte Carlo technique. In particular, when both second- and third-neighbor super-exchanges are considered, we find that a gapped spin liquid described by non-trivial magnetic fluxes and long-range chiral-chiral correlations is energetically favored compared to the gapless U(1) Dirac state. Furthermore, the topological Chern number, obtained by integrating the Berry curvature, and the degeneracy of the ground state, by constructing linearly independent states, lead us to identify this flux state as the chiral spin liquid with $C = 1/2$ fractionalized Chern number.

PACS numbers: 75.10.Jm, 75.10.Kt, 75.40.Mg, 75.50.Ee

Introduction – Quantum spin liquids (QSL) are exotic phases of strongly correlated spin systems, which do not possess any local order even at zero temperature[1] but develop topological order due to the long-range entanglement in the system.[2] Various QSL have been suggested as the ground state of some frustrated magnetic systems,[1] and have been searched for many years in both experimental and theoretical studies. The Kagome antiferromagnet is the most promising system for hosting QSL.[3–22] In the corresponding Heisenberg model on the Kagome lattice with nearest-neighbor interactions, a time-reversal symmetric QSL has been discovered by different advanced numerical methods, with gapped[16–19] or gapless excitations.[13,14]

A sub-class of QSL, which breaks time-reversal symmetry, is called chiral spin liquid (CSL).[23–26] By doping the CSL, the condensation of the anyonic quasi-particles might realize exotic superconductivity.[24,27,28] The simplest CSL is given by the Kalmeyer-Laughlin state, which was proposed as the $\nu = 1/2$ fractional quantum Hall state in frustrated magnetic systems.[23] However, the realization of CSL by a spontaneous time-reversal symmetry breaking in realistic frustrated magnetic systems was elusive in past.[29,30] Recently, the state-of-art density-matrix renormalization group (DMRG) has been implemented to study different spin-1/2 antiferromagnets on Kagome lattice with the spin couplings up to the third neighbors.[20,21] A CSL has been suggested as the $\nu = 1/2$ Laughlin state in these systems, based upon the calculation of the fractionally quantized Chern number $C = 1/2$[20] and chiral edge spectrum.[21] Meanwhile, the same CSL has been also obtained in the Heisenberg model with explicit time-reversal symmetry breaking chiral interactions on the Kagome lattice.[22]

In theoretical studies, Wen *et al.*[24] described the CSL states through the fluxes of an underlying gauge field theory within the fermionic representation, which had shed light on the understanding of the topological order of the CSL, including the topological degeneracy and fractionalized quasi-particles.[2,31–34] Recently, Zhang *et al.*[35] revealed the semionic statistics of quasi-particles for the CSL state on a square lattice using the Gutzwiller projective fermionic representation with the π-flux phase.[24,36] Motivated by the discovery of the CSL in extended Kagome systems,[20,21] recent variational studies based on the Gutzwiller projected parton wave function found that the third-neighbor coupling could stabilize the CSL in the Heisenberg model on the Kagome lattice.[15] This finding stimulates a deeper study and characterization (e.g., topological properties) of variational wave functions. In particular, it is interesting to compare the topological nature of such a CSL in the variational approach with the DMRG results.[20,21,37]

In this paper, we consider both the $J_1-J_2-J_3$ Heisenberg model:

$$H = J_1 \sum_{\langle ij \rangle} \vec{S}_i \cdot \vec{S}_j + J_2 \sum_{\langle\langle ij \rangle\rangle} \vec{S}_i \cdot \vec{S}_j + J_3 \sum_{\langle\langle\langle ij \rangle\rangle\rangle} \vec{S}_i \cdot \vec{S}_j, \quad (1)$$

and the J_1-J_χ model (with explicit chiral interactions):

$$H_\chi = J_1 \sum_{\langle ij \rangle} \vec{S}_i \cdot \vec{S}_j + J_\chi \sum_{\triangle/\triangledown} \vec{S}_i \cdot (\vec{S}_j \times \vec{S}_k), \quad (2)$$

on the Kagome lattice. In the $J_1-J_2-J_3$ model, the system has the first- (J_1), second- (J_2) and third-neighbor (J_3) couplings (the latter ones, only inside each hexagon); while in the J_1-J_χ model, it has the chiral couplings in each up ($\triangle$) and down ($\triangledown$) triangles, and the sites i, j, and k follow the clockwise order in the triangles. In the following, we will take $J_1 = 1$ as the unit of energies.

Variational wave functions are constructed by projecting mean-field states in the fermionic representation. Through careful optimization of the variational parameters and simulations on large clusters, we compare the energies of the U(1) Dirac spin liquid (DSL) and CSL. For the $J_1-J_2-J_3$ model, the CSL overcomes the DSL when J_3 is slightly larger than J_2. We would like to mention

that, with even larger values of J_3, DMRG calculations suggested that the CSL has a transition to another spin ordered phase,[37] but this issue is not addressed in the present paper. For the J_1-J_χ model, a consistent energy gain is obtained for the CSL state at $J_\chi = 0.15$. The chiral-chiral correlation functions show a long-range chiral order, consistent with DMRG results. Most importantly, the calculation of the topological Chern number[26] allows us to conclude that the CSL in both models is equivalent to the $\nu = 1/2$ Laughlin state, as established in DMRG calculations.[20,21] Finally, we show that also the ground-state degeneracy, obtained by considering different boundary conditions in the mean-field Hamiltonian, is consistent with what expected from a CSL.

Method and Wave Function – The variational wave functions are defined by the projected mean-field states:

$$|\Psi_V\rangle = \mathcal{P}_G|\Psi_{MF}\rangle, \tag{3}$$

where $\mathcal{P}_G = \prod_i(1 - n_{i\uparrow}n_{i\downarrow})$ is the Gutzwiller projector, which enforces no double occupation on each site. $|\Psi_{MF}\rangle$ is the ground state of a mean-field Hamiltonian that only contains hopping:

$$H_{MF} = \sum_{ij,\sigma} t_{ij} c^\dagger_{i\sigma} c_{j\sigma} + h.c., \tag{4}$$

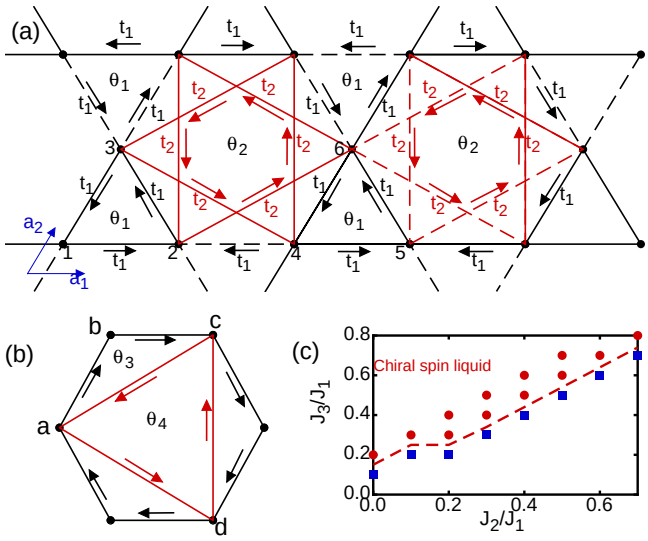

FIG. 1: (Color online) (a) and (b) The variational *Ansatz* with the NN hopping t_1 (black) and NNN hopping t_2 (red) is shown. Solid (dashed) lines indicate positive (negative) hoppings, which define the U(1) DSL. The phases ϕ_1 and ϕ_2 are added upon this *Ansatz* to obtain a CSL. The direction of arrows indicates one possible convention of phases. In each up and down triangle, the flux is $\theta_1 = 3\phi_1$; in each hexagon the flux is $\theta_2 = \pi - 6\phi_1$. The triangle abc has flux $\theta_3 = \pi - 2\phi_1 - \phi_2$, and the triangle acd has flux $\theta_4 = 3\phi_2$. (c) Phase diagram: the red dots (CSL) and blue squares (U(1) DSL) are the calculated data. The red dashed line indicates the approximate phase boundary between the CSL and U(1) DSL.

where $c^\dagger_{i,\sigma}$ ($c_{i,\sigma}$) creates (destroys) an electron on site i with spin σ. Different spin-liquid phases can be described by the different patterns of t_{ij} on the bonds of the lattice. Here, we consider the hoppings for nearest-neighbor (NN) and next-nearest neighbor (NNN) bonds, indicated by t_1 and t_2, respectively. Since we are interested in CSL, we allow for both real and imaginary parts in the hopping i.e., $t_{ij} = |t_{ij}|e^{i\phi_{ij}}$. In Fig. 1, we show the *Ansatz* of our variational wave function; since $t^*_{ij} = t_{ji}$ an orientation of the bond is needed: for the hopping from i to j, t_{ij} (t^*_{ij}) is taken in (opposite to) the direction of the arrow.

Here, we choose the case where the up and down triangles have the same fluxes (i.e., $\theta_1 = 3\phi_1$), and the flux in the hexagon is $\theta_2 = \pi - 6\phi_1$. This state can be represented as $[3\phi_1, \pi - 6\phi_1]$, as considered in Refs. 13 and 15. When including also the NNN bonds, a more complex flux structure appears in the hexagon, as shown in Fig. 1: the triangles abc have flux $\theta_3 = \pi - 2\phi_1 - \phi_2$, and the triangles acd have flux $\theta_4 = 3\phi_2$. Thus, the variational state can be represented by using the four fluxes (θ_i) as $[3\phi_1, \pi - 6\phi_1; \pi - 2\phi_1 - \phi_2, 3\phi_2]$. The U(1) DSL, which has two Dirac point (for each spin), has fluxes $[0, \pi, \pi, 0]$; otherwise, the wave function describes a CSL.[7] In our calculations, we set the real part of the NN hopping $Re(t_1) = 1$, and tune the imaginary part $Im(t_1)$ to change ϕ_1. For each ϕ_1, we optimize the other two parameters (i.e., $Re(t_2)$ and $Im(t_2)$) using variational Monte Carlo to find the energetically favored state. In particular, we use the stochastic reconfiguration (SR) optimization method,[38] which allows us to obtain an extremely accurate determination of variational parameters.

Results – We performed our variational calculations for the mean-field Hamiltonian Eq. (4) at half filling on toric clusters with $L \times L \times 3$ sites under the antiperiodic boundary conditions (APBC), and compared the U(1) DSL and the CSL. We start from the U(1) DSL, and add the fluxes gradually through increasing ϕ_1 to get the CSL. If we only consider the NN hopping term t_1 within the variational wave function, we find that, for $J_2 = J_3 > 0.3$, the CSL appears in the $J_1-J_2-J_3$ Heisenberg model as a local minimum. Most importantly, only when the NNN term t_2 is taken into account, the CSL has an energy gain with respect to the U(1) DSL. Therefore, in the following, we use the wave function including both ϕ_1 and ϕ_2.

Our main results are presented in Fig. 2. For the $J_1-J_2-J_3$ Heisenberg model of Eq. (1), we find that the CSL is energetically favored when J_3 is a little larger than J_2. As an example in Fig. 2(a), we show that, at $J_2 = 0.5$ and $J_3 = 0.6$, the energy exhibits a minimum at a finite value of ϕ_1, which is $\phi_1 = 0.0505\pi$ for $L = 8$ and $\phi_1 = 0.0567\pi$ for $L = 12$ and 16. It is quite time consuming to perform SR optimization on larger sizes, but, fortunately, the variational parameters are only slightly modified from $L = 12$ to $L = 16$ (see supplemental material). Therefore, we take the wave function optimized for $L = 16$ to calculate variational energies up to $L = 36$. After the finite-size scaling, which is shown in the inset of

Fig. 2(a), the estimated energy per site at $J_2 = 0.5$ and $J_3 = 0.6$ is $E = -0.4387(1)$. In this case, the accuracy is about 5.8%, compared with the DMRG data on cylinder geometries (where $E = -0.465603$). By contrast, at $J_2 = J_3 = 0.5$ and up to $L = 12$, the best energy is given by the U(1) DSL, see Fig. 2(b). However, when we take the optimized wave functions at each ϕ_1 and perform the calculations up to $L = 28$, we find that the difference between the energies at $\phi_1 = 0$ and 0.0159π is very small (i.e., of the order of 10^{-4}). Actually, performing the finite size scaling yields the same estimated energy per site $E = -0.4420(1)$, as shown in the insert of Fig. 2(b). This point is very close to the boundary of the phase transition, thus it is hard to distinguish the CSL from the U(1) DSL. More results for different values of J_2 and J_3 are shown in the supplemental material.

The rough phase diagram for the $J_1-J_2-J_3$ Heisenberg model is presented in Fig. 1(c). Here, for $J_2 = 0$, we get the CSL for $J_3 \geq 0.2$, which is different from the conclusion in Ref. 15, which obtained $J_3 > 0.3$. The reason of this discrepancy might be due to the energy gain obtained by including the NNN hopping t_2 in the variational wave function.

In order to detect the chiral order in the optimized wave functions, we measure the chiral-chiral correlation function between two triangles defined as:

$$\langle \chi_i \chi_j \rangle = \langle [\vec{S}_1^i \cdot (\vec{S}_2^i \times \vec{S}_3^i)][\vec{S}_1^j \cdot (\vec{S}_2^j \times \vec{S}_3^j)] \rangle, \qquad (5)$$

where $\chi_i = \vec{S}_1^i \cdot (\vec{S}_2^i \times \vec{S}_3^i)$ is the chirality of triangle $\triangle_{123}^i$. In Fig. 3, we show the chiral-chiral correlation $\langle \chi_i \chi_j \rangle$ as a function of the distance $|i-j|$ between two up triangles at $J_2 = 0.5$ and $J_3 = 0.6$ on $8 \times 8 \times 3$ and $12 \times 12 \times 3$ lattices. On both clusters, $\langle \chi_i \chi_j \rangle$ decays rapidly to a finite value, indicating the long-range chiral order, the difference between $L = 8$ and 12 being small. It is interesting to note that the chiral order is larger in the accurate DMRG calculations (performed cylinder with $L = 6$) than in variational Monte Carlo ones.

The variational state with non-trivial fluxes ($[3\phi_1, \pi - 6\phi_1; \pi - 2\phi_1 - \phi_2, 3\phi_2]$) can be also implemented to the J_1-J_χ model of Eq. (2). In this case, the CSL is stabilized much easier: even for a small value of J_χ, namely $J_\chi = 0.15$, there is a clear minimum in the energy around $\phi_1 = 0.0928\pi$, see Fig. 2(c). For $L = 12$, the CSL has an energy per site $E = -0.45057(1)$, much lower than $E = -0.42872(2)$ of the U(1) DSL. Also the chiral-chiral correlation function in Fig. 3 indicates a robust chiral order at $J_\chi = 0.15$.

Until now, we have shown that the chiral state arises in these two models in view of the chiral-chiral correlation. However, a CSL is further characterized by the non-trivial topological structures, including the topological Chern number[26] and the degeneracy of the ground state.[2] In the following, we proceed in these two directions to clarify that our variational state indeed represents a CSL state.

First, the topological Chern number is computed as the integral over the Berry curvature $F(\Theta_1, \Theta_2)$:[39–42]

$$C = \frac{1}{2\pi} \int d\Theta_1 d\Theta_2 F(\Theta_1, \Theta_2), \qquad (6)$$

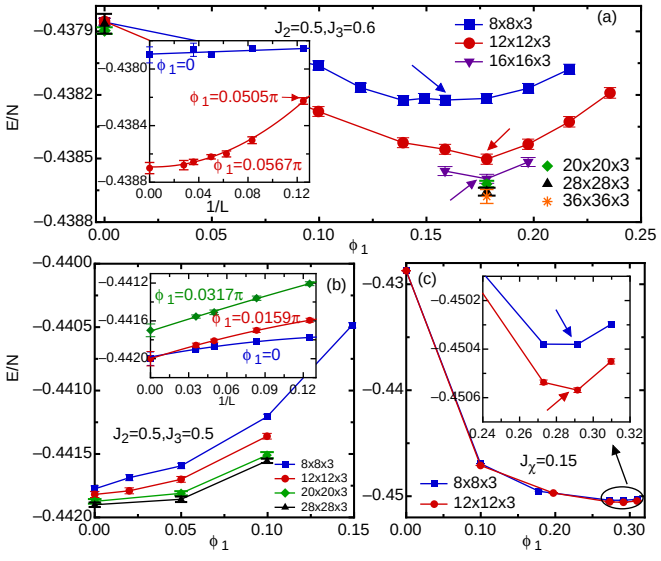

FIG. 2: (Color online) The energy per site as function of ϕ_1 on different lattices. Results for the $J_1-J_2-J_3$ Heisenberg model at $J_2 = 0.5$ with $J_3 = 0.6$ (a) and 0.5 (b), for the J_1-J_χ model at $J_\chi = 0.15$ (c). Insets: the energy per site as function of $1/L$ for the U(1) DSL ($\phi_1 = 0$) up to $L = 28$, and the CSL with $\phi_1 = 0.0505\pi$ on $L = 8$ lattice and $\phi_1 = 0.0567\pi$ on larger clusters up to $L = 36$ (a); the finite size effect for different ϕ_1 (b) and with enlarged scale around $\phi_1 = 0.0928\pi$ (c). The arrows in (a) and (c) show the energy minimum, and indicate the CSL stabilized in both models.

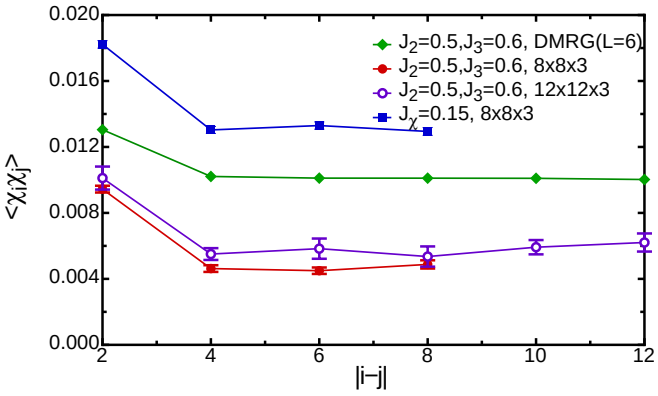

FIG. 3: (Color online) The chiral-chiral correlation function along $\vec{a}_1$ direction on $L = 8$ and 12 lattices for the $J_1-J_2-J_3$ Heisenberg model (at $J_2 = 0.5$ and $J_3 = 0.6$) and the J_1-J_χ model (at $J_\chi = 0.15$). The DMRG data are calculated on cylinder with $L = 6$ at $J_2 = 0.5$ and $J_3 = 0.6$.

where $0 \leq \Theta_k \leq 2\pi$ $(k = 1, 2)$. To compute the Chern number numerically, we consider twisted boundary conditions in the mean-field Hamiltonian, namely $c_{j+L_k\uparrow} = c_{j\uparrow}e^{i\Theta_k}$ and $c_{j+L_k\downarrow} = c_{j\downarrow}e^{-i\Theta_k}$. Then, we divide the the Brillouin zone into M plaquettes, with the Berry curvature being $F_l = arg\prod_i \langle\Psi_V^{l_{i+1}}|\Psi_V^{l_i}\rangle$ $(l = 1, \ldots, M;$ $i = 1, 2, 3, 4$ for the four corners of the l-th plaquette, and $\Psi_V^{l_5} = \Psi_V^{l_1})$, where $|\Psi_V^l\rangle$ is the projected ground state of the mean-field Hamiltonian with twisted boundary conditions. The overlap $\langle\Psi_V^{l_{i+1}}|\Psi_V^{l_i}\rangle = \sum_x P(x)\frac{\langle x|\Psi_V^{l_i}\rangle}{\langle x|\Psi_V^{l_{i+1}}\rangle}$ is calculated by Monte Carlo method according to the weight $P(x) = \frac{|\langle x|\Psi_V^{l_{i+1}}\rangle|^2}{\sum_x |\langle x|\Psi_V^{l_{i+1}}\rangle|^2}$. In order to numerically check the accuracy, we changed M from 100 up to 400 plaquettes. The numerical results show that the dimension of mesh changes the Berry curvature, but gives the same topological Chern number. We must emphasize that the integration from 0 to 2π in the twist of the fermionic operators includes two periods of phases for the spin operators and, therefore, the result must be divided by 4. The integration between 0 and 2π gives 2 with high accuracy (see Fig. 4), leading to $C = 1/2$, which is fully consistent with recent DMRG results.[20]

The degeneracy of the wave function, which indicates non-trivial ground-state structure, was not obvious to obtain from the variational approach with the Gutzwiller projected parton construction. Recently, Zhang *et al.*[35] realized that the ground-state degeneracy is consistent with the linear dependence for variational wave functions through fermionic construction for SU(2) Chern-Simons theory. We follow the same idea to construct the linearly independent states from the four projected states that are obtained through changing the boundary conditions of the mean field Hamiltonian in $\vec{a}_1$ and $\vec{a}_2$ directions

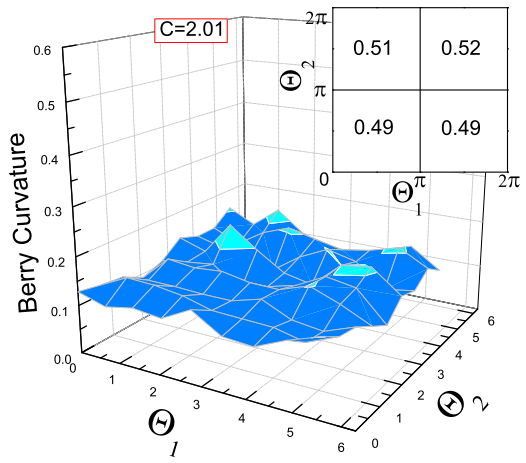

FIG. 4: (Color online) The Berry curvature at $J_2 = 0.5$ and $J_3 = 0.6$ on $L = 12$ lattice. The Brillouin zone is divided into a mesh with 100 plaquettes. The summation between 0 and 2π gives $C = 2.01$.

(see Fig. 1). We denote the four states as $|\psi_1, \psi_2\rangle$, where $\psi_i = 0$ for periodic boundary condition and π for antiperiodic boundary condition $(i = 1, 2)$. In order to find the linearly independent states from these four projected states (i.e., $\{|0,0\rangle, |0,\pi\rangle, |\pi,0\rangle, |\pi,\pi\rangle\}$), we calculate the overlaps between all possible states. The numerical calculations up to $L = 32$ indicate strong size effects, due to the smallness of the mean-field gap. For example, for $J_2 = 0.5$ and $J_3 = 0.6$ on the $16 \times 16 \times 3$ lattice with $\phi_1 = 0.0567\pi$ and $\phi_2 = -0.2807\pi$, the band gap is only about 0.6.

Thus, in order to suppress the finite-size effects on small clusters, we tune ϕ_1 and ϕ_2 to enlarge the mean-field band gap (up to a value of 2), still keeping the long-range chiral order and a non-zero Chern number. Consequently, even on the small $8 \times 8 \times 3$ lattice, we find the two linear independent states indicating the two-fold degeneracy, which are (see the supplemental material for details):

$$|1\rangle = |00\rangle = \frac{1}{\sqrt{3}}(|0,\pi\rangle + |\pi,0\rangle + |\pi,\pi\rangle), \quad (7)$$

$$|2\rangle = \frac{1}{\sqrt{6}}(|0,\pi\rangle + e^{i\frac{2\pi}{3}}|\pi,0\rangle + e^{-i\frac{2\pi}{3}}|\pi,\pi\rangle). \quad (8)$$

Conclusions – In conclusion, we investigated the CSL in the $J_1-J_2-J_3$ Heisenberg models on the Kagome lattice by the variational approach with Gutzwiller projected fermionic construction. Our variational studies reveal that the CSL is energetically favored in the phase region consistent with the recent DMRG calculations.[20] However, differently from the DMRG results, we found that when J_3 is larger than J_2, instead of $J_2 = J_3$, the CSL begins to appear as indicated by the existence of energy minimum while tuning the fluxes. On the other hand, we have shown that our wave function also works for the $J_1 - J_\chi$ model, which includes a three-spin parity and time reversal violating interaction.

Further investigations with these optimized wave functions show that the spin-spin correlation functions decay fast (see supplemental material), indicating short-range correlations. Instead, the chiral-chiral correlation function presents a long-range chiral order, consistent with DMRG results. The variational wave function underestimates the robust of the CSL, as the accurate DMRG calculations show stronger chiral order than variational state. Moreover, our calculations of the topological Chern number and the ground state degeneracy suggest that the chiral state is the $\nu = 1/2$ Laughlin state.

Acknowledgements – W.-J.H. and F.B. thank D. Poilblanc and Y. Iqbal for useful discussions. This research is supported by the National Science Foundation through grants DMR-1408560 (W.-J.H, D.N.S), DMR-1205734 (S.S.G.), and U.S. Department of Energy, Office of Basic Energy Sciences under grant No. DE-FG02-06ER46305 (W.Z.). Y.Z. is supported by SITP. F.B. by PRIN 2010-11.

[1] L. Balents, Nature (London) **464**, 199 (2010).
[2] X.-G. Wen, Phys. Rev. B **40**, 7387 (1989); X.-G. Wen, Int. J. Mod. Phys. B **4**, 239 (1990); X.-G. Wen and Q. Niu, Phys. Rev. B **41**, 9377 (1990).
[3] P.A. Lee, Science **321**, 1306 (2008).
[4] P. Mendels and F. Bert, J. Phys. Conf. Ser. **320**, 012004 (2011).
[5] T.-H. Han, J. S. Helton, S. Chu, D. G. Nocera, J. A. Rodriguez-Rivera, C. Broholm, and Y. S. Lee, Nature **492**, 406 (2012).
[6] J. Marston and C. Zeng, J. Appl. Phys. **69**, 5962 (1991).
[7] M.B. Hastings, Phys. Rev. B **63**, 014413 (2000).
[8] L. Balents, M.P.A. Fisher, and S.M. Girvin, Phys. Rev. B **65**, 224412 (2002).
[9] F. Wang and A. Vishwanath, Phys. Rev. B **74**, 174423 (2006).
[10] M. Hermele, Y. Ran, P.A. Lee, and X.-G. Wen, Phys. Rev. B **77**, 224413 (2008).
[11] Y.-M. Lu, Y. Ran, and P.A. Lee, Phys. Rev. B **83**, 224413 (2011); Y.-M. Lu, G. Y. Cho, and A. Vishwanath, arXiv: 1403.0575.
[12] L. Messio, B. Bernu, and C. Lhuillier, Phys. Rev. Lett. **108**, 207204 (2012).
[13] Y. Ran, M. Hermele, P.A. Lee, and X.-G. Wen, Phys. Rev. Lett. **98**, 117205 (2007).
[14] Y. Iqbal, F. Becca, and D. Poilblanc, Phys. Rev. B **84**, 020407 (2011); Y. Iqbal, F. Becca, S. Sorella, and D. Poilblanc, Phys. Rev. B **87**, 060405 (2013); Y. Iqbal, D. Poilblanc, and F. Becca, Phys. Rev. B **89**, 020407 (2014).
[15] J.-W. Mei and X.-G. Wen, arXiv:1407.0869.
[16] H.C. Jiang, Z.Y. Weng, and D.N. Sheng, Phys. Rev. Lett. **101**, 117203 (2008).
[17] S. Yan, D. Huse, and S. White, Science **332**, 1173 (2011).
[18] S. Depenbrock, I.P. McCulloch, and U. Schollwöck, Phys. Rev. Lett. **109**, 067201 (2012).
[19] H.C. Jiang, Z. Wang, and L. Balents, Nat. Phys. **8**, 902 (2012).
[20] S.S. Gong, W. Zhu, and D.N. Sheng, Scientific Reports **4**, 6317 (2014).
[21] Y.C. He, D.N. Sheng, and Y. Chen, Phys. Rev. Lett. **112**, 137202 (2014).
[22] B. Bauer, B.P. Keller, M. Dolfi, S. Trebst, and A.W.W. Ludwig, arXiv:1303.6963; B. Bauer, L. Cincio, B.P. Keller, M. Dolfi, G. Vidal, S. Trebst, and A.W.W. Ludwig, arXiv:1401.3017.
[23] V. Kalmeyer and R.B. Laughlin, Phys. Rev. B **39**, 11879 (1989).
[24] X.-G. Wen, F. Wilczek, and A. Zee, Phys. Rev. B **39**, 11413 (1989).
[25] K. Yang, L.K. Warman, and S.M. Girvin, Phys. Rev. Lett. **70**, 2641 (1993).
[26] F.D.M. Haldane and D.P. Arovas, Phys. Rev. B **52**, 4223 (1995).
[27] R.B. Laughlin, Phys. Rev. Lett. **60**, 2677 (1988).
[28] F. Wilczek, Fractional Statistics and Anyon Superconductivity (World Science, Singapore, 1990).
[29] D.F. Schroeter, E. Kaplt, R. Thomale, and M. Grelter, Phys. Rev. Lett. **99**, 097202 (2007).
[30] A.E.B. Nielsen, J.I. Cirac, and G. Sierra, Phys. Rev. Lett. **108**, 257206 (2012).
[31] F. Wilczek and A. Zee, Phys. Rev. Lett. **52**, 2111 (1984).
[32] R.B. Laughlin, Phys. Rev. Lett. **50**, 1395 (1983).
[33] D. Arovas, J.R. Schrieffer, and F. Wilczek, Phys. Rev. Lett. **53**, 722 (1984).
[34] X.-G. Wen, Phys. Rev. B **44**, 2664 (1991).
[35] Y. Zhang, T. Grover, and A. Vishwanath, Phys. Rev. B **84**, 075128 (2011); Y. Zhang, T. Grover, A. Turner, M. Oshikawa, and A. Vishwanath, Phys. Rev. B **85**, 235151 (2012); Y. Zhang and A. Vishwanath, Phys. Rev. B **87**, 161113 (2013).
[36] A.W.W. Ludwig, M.P.A. Fisher, R. Shankar, and G. Grinstein, Phys. Rev. B **50**, 7526 (1994).
[37] S.S. Gong, W. Zhu, L. Balents, and D.N. Sheng, in preparation.
[38] S. Sorella, Phys. Rev. B **71**, 241103 (2005).
[39] Q. Niu, D.J. Thouless, and Y.-S. Wu, Phys. Rev. B **31**, 3372 (1985).
[40] D.N. Sheng, Xin Wan, E.H. Rezayi, Kun Yang, R.N. Bhatt, and F.D.M. Haldane, Phys. Rev. Lett. **90**, 256802 (2003).
[41] X. Wan, D.N. Sheng, E.H. Rezayi, Kun Yang, R.N. Bhatt, and F.D.M. Haldane, Phys. Rev. B **72**, 075325 (2005).
[42] M. Hafezi, A.S. Sorensen, M.D. Lukin, and E. Demler, Europhys. Lett. **81**, 1005 (2008)

Supplemental Material

More energy data and spin-spin correlation functions — We show the energy per site at different values of J_2 and J_3 with antiperiodic (APBC) and periodic (PBC) boundary conditions in Fig. 5. On the $4\times4\times3$ lattice, the results depend on different boundary conditions, owing to finite-size effect. As the size is increased to the $8\times8\times3$ lattice, the energy per site only exhibits slight difference under different boundary conditions (of the order of 10^{-4}). On larger clusters, the energy results with different boundary conditions are the same within one error bar. The optimized values of the phases ϕ_1 and ϕ_2 for the wave functions with APBC and PBC are reported in Table I. By taking the wave functions optimized on the $12\times12\times3$ or $16\times16\times3$ lattice, we perform variational calculations up to $36\times36\times3$ lattice, and perform the finite-size scaling to obtain the estimated energies (see the insets of Fig. 5).

Fig. 6 shows several calculations on the $8\times8\times3$ lattice with APBC at different J_2 and J_3, qualitatively similar results are obtained with different boundary conditions. The CSL is energetically favored when the energy per site decreases as the flux ϕ_1 is increased. The schematic phase diagram shown in the main text is constructed from these results.

Taking the optimized variational wave function on the $16\times16\times3$ lattice, we measure the spin-spin correlation function, see Fig. 7 that also shows a comparison with DMRG results on cylinder with $L=4$. The fast decay of the spin correlation indicates the absence of a long-range order, consistent with DMRG conclusions.

Details for the degeneracy — In order to find the linearly independent ground states, we numerically calculate all the overlaps between states with different boundary conditions in the mean-field Hamiltonian, which are indicated by $\{|\psi_1,\psi_2\rangle\}=\{|0,0\rangle,|0,\pi\rangle,|\pi,0\rangle,|\pi,\pi\rangle\}$. In order to maximize the mean-field gap, i.e., $\Delta\simeq2$, we take $\phi_1=0.1015\pi$ and $\phi_2=0.25\pi$ and perform the calculations on the $8\times8\times3$ lattice. By fixing the global phases in such a way that all the overlaps with $|0,0\rangle$ are real, we get the overlap matrix $\mathcal{O}$:[35]

$$\begin{aligned}\mathcal{O} &= \begin{pmatrix} \langle0,0|0,0\rangle & \langle0,0|0,\pi\rangle & \langle0,0|\pi,0\rangle & \langle0,0|\pi,\pi\rangle \\ \langle0,\pi|0,0\rangle & \langle0,\pi|0,\pi\rangle & \langle0,\pi|\pi,0\rangle & \langle0,\pi|\pi,\pi\rangle \\ \langle\pi,0|0,0\rangle & \langle\pi,0|0,\pi\rangle & \langle\pi,0|\pi,0\rangle & \langle\pi,0|\pi,\pi\rangle \\ \langle\pi,\pi|0,0\rangle & \langle\pi,\pi|0,\pi\rangle & \langle\pi,\pi|\pi,0\rangle & \langle\pi,\pi|\pi,\pi\rangle \end{pmatrix} \\ &\approx \begin{pmatrix} 1 & 0.57 & 0.57 & 0.57 \\ 0.57 & 1 & 0.57e^{-i1.6} & 0.58e^{i1.6} \\ 0.57 & 0.57e^{i1.6} & 1 & 0.57e^{-i1.6} \\ 0.57 & 0.57e^{-i1.6} & 0.57e^{i1.5} & 1 \end{pmatrix} \\ &\approx \begin{pmatrix} 1 & \frac{1}{\sqrt3} & \frac{1}{\sqrt3} & \frac{1}{\sqrt3} \\ \frac{1}{\sqrt3} & 1 & -\frac{i}{\sqrt3} & \frac{i}{\sqrt3} \\ \frac{1}{\sqrt3} & \frac{i}{\sqrt3} & 1 & -\frac{i}{\sqrt3} \\ \frac{1}{\sqrt3} & -\frac{i}{\sqrt3} & \frac{i}{\sqrt3} & 1 \end{pmatrix}. \end{aligned} \tag{9}$$

The independent ground states can be found by diagonalizing the overlap matrix, i.e., $\mathcal{O}=U^\dagger\Lambda U$. We find that only two eigenvalues are non-zero, indicating that only two eigenvectors are linearly independent. This fact implies that the ground-state degeneracy is two-fold. In particular, these two states can be constructed such to preserve lattice symmetries. For example, we can consider the $2\pi/3$ rotations, generated by the operator $R_{2\pi/3}$. Within the Gutzwiller projected fermionic representation, the four wave functions from different boundary conditions have the following relations under $R_{2\pi/3}$ rotations:

$$\begin{aligned} R_{2\pi/3}|00\rangle &= |00\rangle, \\ R_{2\pi/3}|0\pi\rangle &= |\pi0\rangle, \\ R_{2\pi/3}|\pi0\rangle &= |\pi\pi\rangle, \\ R_{2\pi/3}|\pi\pi\rangle &= |0\pi\rangle. \end{aligned}$$

Eigenstates of $R_{2\pi/3}$ can be easily constructed, with eigenvalues $r=1$, $r=e^{-\frac{2\pi i}{3}}$, and $r=e^{\frac{2\pi i}{3}}$:

$$\begin{aligned} R_{2\pi/3}\ &:\ r=1 \\ &\quad |1\rangle=|00\rangle, \\ R_{2\pi/3}\ &:\ r=e^{-\frac{2\pi i}{3}} \\ &\quad |2\rangle\propto|0\pi\rangle+e^{\frac{2\pi i}{3}}|\pi0\rangle+e^{-\frac{2\pi i}{3}}|\pi\pi\rangle, \\ R_{2\pi/3}\ &:\ r=e^{\frac{2\pi i}{3}} \\ &\quad |3\rangle\propto|0\pi\rangle+e^{-\frac{2\pi i}{3}}|\pi0\rangle+e^{\frac{2\pi i}{3}}|\pi\pi\rangle, \\ R_{2\pi/3}\ &:\ r=1 \\ &\quad |4\rangle\propto|0\pi\rangle+|\pi0\rangle+|\pi\pi\rangle. \end{aligned}$$

Our numerical results of Eq. (9) imply that only two linearly independent states exist:

$$|1\rangle=|00\rangle, \tag{10}$$

$$|2\rangle=\frac{1}{\sqrt6}(|0,\pi\rangle+e^{\frac{2\pi i}{3}}|\pi,0\rangle+e^{-\frac{2\pi i}{3}}|\pi,\pi\rangle), \tag{11}$$

$$|3\rangle=\varnothing, \tag{12}$$

$$|4\rangle=\frac{1}{\sqrt3}(|0,\pi\rangle+|\pi,0\rangle+|\pi,\pi\rangle)=|1\rangle. \tag{13}$$

Therefore, the four projected states $\{|\psi_1,\psi_2\rangle\}$ can be represented by using the two independent states $|1\rangle$ and $|2\rangle$:

$$\begin{aligned} |00\rangle &= |1\rangle\,, \\ |0\pi\rangle &= \frac{1}{\sqrt3}|1\rangle+\sqrt{\frac{2}{3}}|2\rangle\,, \\ |\pi0\rangle &= \frac{1}{\sqrt3}|1\rangle+\sqrt{\frac{2}{3}}e^{-\frac{2\pi i}{3}}|2\rangle\,, \\ |\pi\pi\rangle &= \frac{1}{\sqrt3}|1\rangle+\sqrt{\frac{2}{3}}e^{\frac{2\pi i}{3}}|2\rangle\,. \end{aligned}$$

Relation between the ground states and the minimum entropy states — In this part, we want to find the relation between the two linearly independent states $|1\rangle$ and $|2\rangle$ of Eqs. (10) and (11) and the minimum entropy

states (MESs).[35] The MESs are the useful basis of the degenerate ground-state manifold for topological ordered phases and label the eigenstates with different quasiparticles threaded through the non-contractible loop along a given direction. The transformation between the MES bases along different directions connected by a symmetry rotation is encoded in the corresponding modular matrix.[35]

Since the Kagome lattice is symmetric under $2\pi/3$ rotation $R_{2\pi/3}$ and the topological order involve no symmetry breaking, the overall ground-state manifold is invariant under $R_{2\pi/3}$. Nevertheless, each individual ground state may still transform differently under $R_{2\pi/3}$, which can be interpreted as a conformal transformation: $(\vec{w}_1, \vec{w}_2)^T \to (\vec{w}_2, \vec{w}_3)^T = (\vec{w}_2, -\vec{w}_1 - \vec{w}_2)^T$, where

$$\begin{aligned} \vec{w}_1 &= \hat{x}, \\ \vec{w}_2 &= \left(-\hat{x} + \sqrt{3}\hat{y}\right)/2, \\ \vec{w}_3 &= \left(-\hat{x} - \sqrt{3}\hat{y}\right)/2, \end{aligned}$$

are three directional vectors along the Bravais lattice vectors.

Therefore, on the Kagome lattice, the $R_{2\pi/3}$ rotation leads to the modular transformation $\mathcal{SU}$ on MESs.[35] For the CSL phase (e.g., the $\nu = 1/2$ Laughlin state), we have the modular $\mathcal{SU}$ matrix:

$$\mathcal{S} = \frac{1}{\sqrt{2}} \begin{pmatrix} 1 & 1 \\ 1 & -1 \end{pmatrix}, \tag{14}$$

$$\mathcal{U} = \begin{pmatrix} 1 & 0 \\ 0 & i \end{pmatrix} e^{-\frac{2\pi i}{24}}, \tag{15}$$

where the phase factor in the definition of $\mathcal{U}$ is given by the chiral edge central charge. The first and the second columns (rows) are the identity particle and the semion quasi-particle, respectively. Physically, for Abelian topological orders, the modular $\mathcal{S}$ matrix determines the mutual statistics of a given quasi-particle encircling around another one, while the modular $\mathcal{U}$ matrix contains the self-statistics of the each quasi-particle.

With the modular $\mathcal{SU}$ matrix as the $2\pi/3$ rotation operator, we can obtain the MESs along the $\vec{w}_2$ and $\vec{w}_3$ directions $\Xi_{1,\vec{w}_2}$ and $\Xi_{1,\vec{w}_3}$ in terms of the MESs along the $\vec{w}_1$ direction $\Xi_{1,\vec{w}_1}$, i.e., $\Xi_{1,\vec{w}_2} = \mathcal{SU}\Xi_{1,\vec{w}_1}$ and $\Xi_{1,\vec{w}_3} = \mathcal{SU}\Xi_{1,\vec{w}_2}$. Similarly, we can construct the other set of MESs $\Xi_{s,\vec{w}_1}$, $\Xi_{s,\vec{w}_2}$, and $\Xi_{s,\vec{w}_3}$:

MES direction	$\Xi_{1,\vec{w}_i}$	$\Xi_{s,\vec{w}_i}$
$\vec{w}_1$	$(1,0)^T$	$(0,1)^T$
$\vec{w}_2$	$(1,1)^T e^{-\pi i/12}/\sqrt{2}$	$(1,-1)^T e^{5\pi i/12}/\sqrt{2}$
$\vec{w}_3$	$(i,1)^T e^{-5\pi i/12}/\sqrt{2}$	$(1,i)^T e^{-\pi i/12}/\sqrt{2}$

Since under $R_{2\pi/3}$ rotations, $\vec{w}_1 \to \vec{w}_2$, $\vec{w}_2 \to \vec{w}_3$ and $\vec{w}_3 \to \vec{w}_1$, we may construct its eigenstates as the following:

$$\begin{aligned} R_{2\pi/3} &: r = 1 : \\ |1\rangle_R &\propto \Xi_{1,\vec{w}_1} + \Xi_{1,\vec{w}_2} + \Xi_{1,\vec{w}_3} \\ &\propto (1 + \frac{e^{-\frac{\pi i}{12}} + e^{\frac{\pi i}{12}}}{\sqrt{2}}, \frac{e^{-\frac{\pi i}{12}} + e^{-\frac{5\pi i}{12}}}{\sqrt{2}})^T \\ &\propto (1 + \sqrt{2}\cos\frac{\pi}{12}, (1-i)\cos\frac{\pi}{6})^T, \end{aligned} \tag{16}$$

$$\begin{aligned} R_{2\pi/3} &: r = e^{-\frac{2\pi i}{3}} : \\ |2\rangle_R &\propto \Xi_{1,\vec{w}_1} + e^{\frac{2\pi i}{3}}\Xi_{1,\vec{w}_2} + e^{-\frac{2\pi i}{3}}\Xi_{1,\vec{w}_3} \\ &\propto (1 + \frac{e^{\frac{7\pi i}{12}} + e^{-\frac{7\pi i}{12}}}{\sqrt{2}}, \frac{e^{\frac{7\pi i}{12}} + e^{\frac{11\pi i}{12}}}{\sqrt{2}})^T \\ &\propto (1 - \sqrt{2}\sin\frac{\pi}{12}), (-1+i)\cos\frac{\pi}{6})^T, \end{aligned} \tag{17}$$

$$\begin{aligned} R_{2\pi/3} &: r = e^{\frac{2\pi i}{3}} : \\ |3\rangle_R &\propto \Xi_{1,\vec{w}_1} + e^{-\frac{2\pi i}{3}}\Xi_{1,\vec{w}_2} + e^{\frac{2\pi i}{3}}\Xi_{1,\vec{w}_3} \\ &\propto (1 + \frac{e^{-\frac{3\pi i}{4}} + e^{\frac{3\pi i}{4}}}{\sqrt{2}}, \frac{e^{-\frac{3\pi i}{4}} + e^{\frac{\pi i}{4}}}{\sqrt{2}})^T \\ &= \varnothing, \end{aligned} \tag{18}$$

which are consistent with the requirement that the ground states are only two-fold degenerate (similar results are obtained by using $\Xi_{s,\vec{w}_i}$).

From Eqs. (10), (11), (16), and (17), we have that:

$$\begin{aligned} |1\rangle_R &= |1\rangle \\ &\propto (1 + \sqrt{2}\cos\frac{\pi}{12}, (1-i)\cos\frac{\pi}{6})^T \\ &\propto |0,\pi\rangle + |\pi,0\rangle + |\pi,\pi\rangle \propto |0,0\rangle, \\ |2\rangle_R &= |2\rangle \\ &\propto (1 - \sqrt{2}\sin\frac{\pi}{12}, (-1+i)\cos\frac{\pi}{6})^T \\ &\propto |0,\pi\rangle + e^{\frac{2\pi i}{3}}|\pi,0\rangle + e^{-\frac{2\pi i}{3}}|\pi,\pi\rangle), \\ |3\rangle_R &= |3\rangle \\ &\propto |0,\pi\rangle + e^{-\frac{2\pi i}{3}}|\pi,0\rangle + e^{\frac{2\pi i}{3}}|\pi,\pi\rangle \\ &\propto \varnothing. \end{aligned}$$

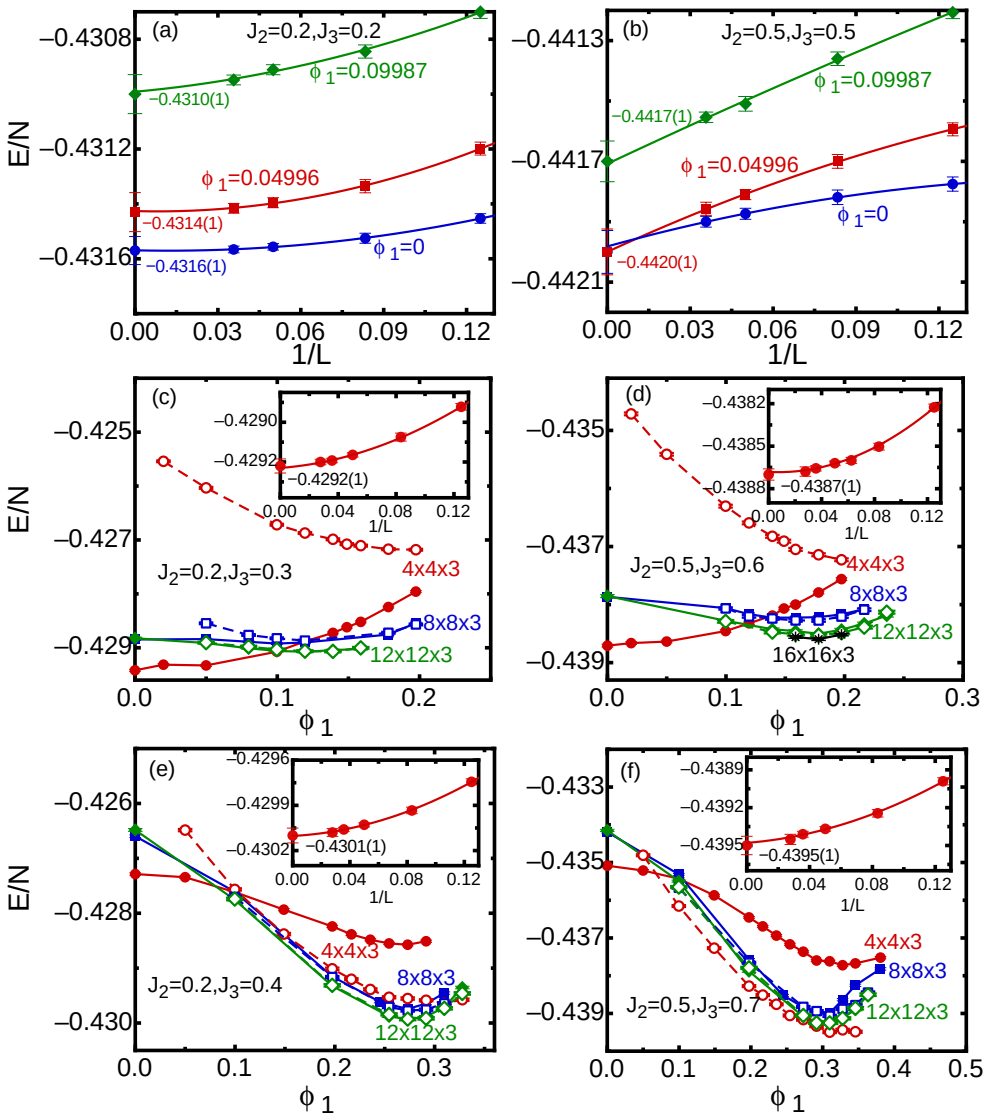

FIG. 5: (Color online) The energy per site on different lattices. The finite-size scaling and different flux ϕ_1 is shown for $J_3 = J_2 = 0.2$ (a) and $J_3 = J_2 = 0.5$ (b). Energy per site as a function of ϕ_1 for different values of J_2 and J_3 are reported in (c), (d), (e), and (f), for various sizes of the cluster: $4 \times 4 \times 3$ (red circles), $8 \times 8 \times 3$ (blue squares), $12 \times 12 \times 3$ (green diamonds), and $16 \times 16 \times 3$ (black stars). The filled (empty) points with solid (dashed) lines indicate APBC (PBC). The insets show the finite size scaling.

TABLE I: We list the fluxes ϕ_1 and ϕ_2 from the best chiral states in Fig. 5 for different values of J_2 and J_3 on different sizes with APBC and PBC.

$APBC$		$N=48$		$N=192$		$N=432$		$N=768$	
J_1	J_2	ϕ_1	ϕ_2	ϕ_1	ϕ_2	ϕ_1	ϕ_2	ϕ_1	ϕ_2
0.2	0.3	0	0	0.0032π	-0.3387π	0.0380π	-0.3801π		
0.2	0.4	0.0869π	-0.6100π	0.0869π	-0.6117π	0.0869π	-0.6150π		
0.5	0.6	0	0	0.0505π	-0.2332π	0.0567π	-0.2802π	0.0567π	-0.2807π
0.5	0.7	0.1043π	-0.6071π	0.0986π	-0.5755π	0.0986π	-0.5803π		
PBC		$N=48$		$N=192$		$N=432$		$N=768$	
J_1	J_2	ϕ_1	ϕ_2	ϕ_1	ϕ_2	ϕ_1	ϕ_2	ϕ_1	ϕ_2
0.2	0.3			0.0032π	-0.3347π	0.0380π	-0.3805π		
0.2	0.4			0.0869π	-0.6138π	0.0869π	-0.6154π		
0.5	0.6			0.0505π	-0.2390π	0.0567π	-0.2785π		
0.5	0.7			0.0986π	-0.5780π	0.0986π	-0.5805π		

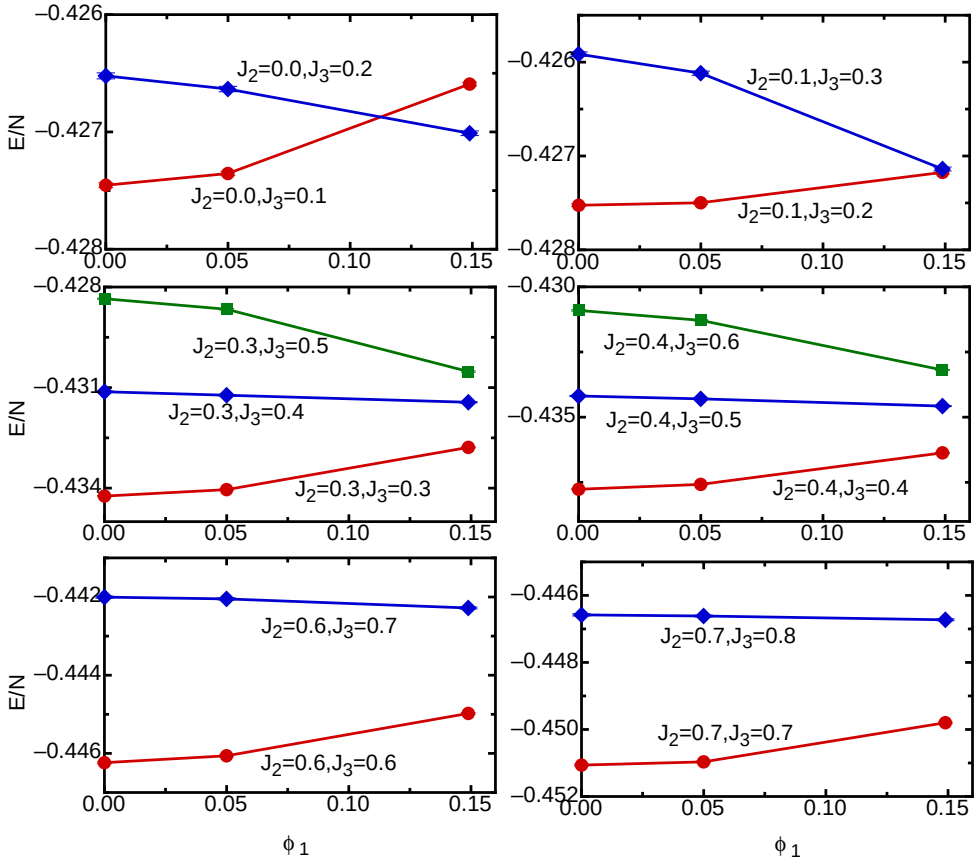

FIG. 6: (Color online) The energy per site at different J_2 and J_3 on the $8 \times 8 \times 3$ lattice. A CSL is energetically favored when the energy per site shows a minimum as a function of ϕ_1.

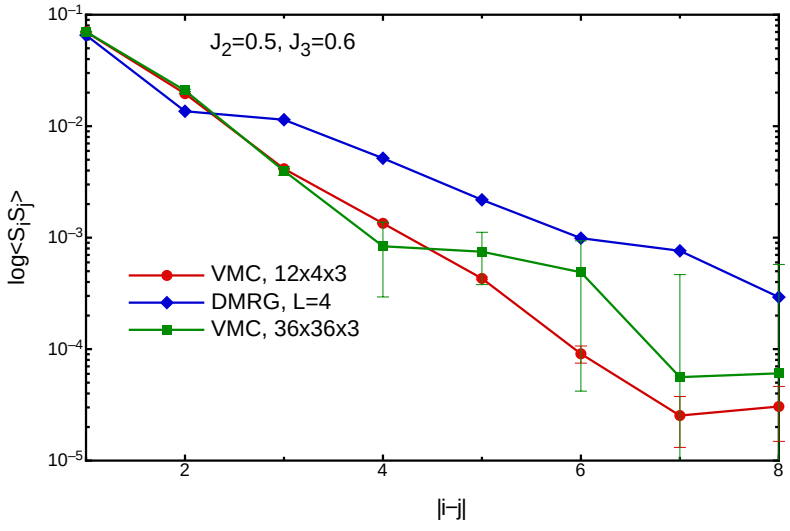

FIG. 7: (Color online) The spin-spin correlation function along the $\vec{a}_1$ direction for $J_2 = 0.5$ and $J_3 = 0.6$ is shown for the variational Monte Carlo (VMC) and density-matrix renormalization group (DMRG) calculations.